



Electrochemical transformation of Fe-N-C catalysts into iron oxides in alkaline medium and its impact on the oxygen reduction reaction activity

Ricardo Sgarbi^{a,b,1}, Kavita Kumar^{a,1}, Viktoriia A. Saveleva^c, Laetitia Dubau^a, Raphaël Chattot^c, Vincent Martin^a, Michel Mermoux^a, Pierre Bordet^d, Pieter Glatzel^c, Edson A. Ticianelli^b, Frédéric Jaouen^e, Frédéric Maillard^{a,b,*}

^a Univ. Grenoble Alpes, Univ. Savoie Mont Blanc, CNRS, Grenoble INP, LEPMI, 38000 Grenoble, France

^b Instituto de Química de São Carlos, Universidade de São Paulo, 13560-960 São Carlos, SP, Brazil

^c ESRF – The European Synchrotron, 71 Avenue des Martyrs, 38000 Grenoble, France

^d Univ. Grenoble Alpes, CNRS, Institut Néel, F-38000 Grenoble, France

^e ICGM, Univ. Montpellier, CNRS, ENSCM, 1919 route de Mende, 34293 Montpellier, France

ARTICLE INFO

Keywords:

Metal-N-C catalyst
Earth-abundant metal catalyst
Fe oxide formation
Oxygen reduction reaction
Anion-exchange membrane fuel cell

ABSTRACT

Precious metal-free Fe-N-C catalysts efficiently electrocatalyze the oxygen reduction reaction both in acid and alkaline electrolyte. Their stability is however limited in acidic medium, but generally accepted to be much higher in alkaline electrolyte. Herein, by combining advanced electron and X-ray based techniques, we provide comprehensive evidence of a Fe dissolution/precipitation mechanism, which partially transforms single Fe atoms into Fe oxide nanoparticles and Fe carbide nanoparticles into Fe carbide core@Fe oxide shell nanoparticles, and is independent on the gas atmosphere used during the accelerated stress tests. Our work shows that Fe-N-C materials based on zero-valent Fe nanoparticles should be designed so that all Fe nanoparticles are protected by a defect-free graphite shell, for improved durability. For single atom Fe-N-C catalysts, the present study raises the question of a possible synergy between minute amount of Fe oxide nanoparticles and Fe-N_xC_y single-atom sites, leading to the higher apparent durability of this catalyst.

1. Introduction

Electrochemical energy conversion devices are promising systems for the world transition from fossil to renewable energies. Among these systems, fuel cells convert efficiently and, in a carbon-neutral manner the chemical energy of a fuel (e.g. hydrogen, H₂) into electricity, provided the fuel is produced from sustainable resources (e.g. via water electrolysis using renewable energy). Acidic fuel cells (proton-exchange membrane fuel cell; PEMFC) are at a more advanced stage of development than anion-exchange membrane fuel cells (AEMFC), but the widespread commercialization of the former is impeded by the high cost of their constituting materials, in particular by the platinum (Pt) nanoparticles (NPs) supported onto high surface area carbon (Pt/C). While Pt/C is used at both electrodes, the Pt loading is mainly at the cathode, due to the sluggish oxygen reduction reaction (ORR) in acid. Approaches pursued to decrease the loading of Pt at the cathode are essentially

focused on alloying Pt with less expensive transition metal elements (e.g. Co, Ni, Cu) [1–7] or lanthanides (e.g. Y, Gd, Pr) [8–11] or substituting Pt with platinum group metal (PGM)-free catalysts such as transition metals (Fe, Co, Sn) embedded in a carbon matrix (C) doped with nitrogen (N) [12,13]. Nevertheless, both PGM-containing and PGM-free catalysts suffer from corrosion of the carbon support/carbon matrix, metal NP/single metal atom detachment, and metal dissolution in PEMFC cathode operating conditions, leading to a loss of active sites and to a drop of the ORR activity of the cathode over time [1–3,14–20].

In contrast, in alkaline media, many oxides of abundant metals are thermodynamically stable, [21] and the formation of carbonates passivates carbon, thus slowing down the CO₂ evolution rate [22,23]. Electrocatalyzing the ORR is also generally more facile in alkaline than in acid (except for Pt) due to the suggested possibility for both inner and outer-sphere electron transfer mechanisms to take place [24]. Recently, we reported that, in alkaline electrolyte, catalysts based on metal NPs

* Corresponding author at: Univ. Grenoble Alpes, Univ. Savoie Mont Blanc, CNRS, Grenoble INP, LEPMI, 38000 Grenoble, France.

E-mail address: frederic.maillard@lepmi.grenoble-inp.fr (F. Maillard).

¹ These authors contributed equally to this work.

surrounded by a N-C shell (Metal@N-C, with Metal = Fe or Co) feature slightly higher ORR mass activity (MA) than some Metal-N-C catalysts with atomically-dispersed Metal-N_xC_y sites (Metal = Fe, Co), [25] and carbon-supported Pt NPs (Pt/C) [26–31]. The Fe-N-C materials are also tolerant to anodic fuels (such as alcohols and borohydride) [28,31–33] and to common contaminants and impurities, which are present in reformed H₂ or in air [13,34]. Thus, the interest in Metal-N-C catalysts for application in AEMFCs is rapidly rising, with recently reported high performance [33,35–39].

The advantage of Metal-N-C catalysts over PGM-containing catalysts in alkaline electrolyte is not limited to the first few hours of operation but extends far beyond that. Using the protocols from the Fuel Cell Commercialization Conference of Japan (FCCJ) [40], Zadick *et al.* [41] and Lafforgue *et al.* [42] reported severe degradation of PGM NPs supported on high surface area carbon. Identical-location transmission electron microscopy studies (IL-TEM) and *in situ* Fourier-transform infrared spectroscopy measurements provided evidence of PGM-catalyzed corrosion of the carbon support leading to detachment of the PGM NPs at potentials higher than 0.6 V vs. the reversible hydrogen electrode (RHE) [43]. It was shown that the ability to corrode carbon depends on the nobleness of the metal NPs and decreases in the order: Pt > PtRu > Pd > Ni [43,44]. In contrast, only a mild decrease of the half-wave potential was reported after accelerated stress tests (ASTs) on Metal-N-C catalysts [26,45,46]. Yet, the most resistant site structure within Fe-N-C catalysts remains an open question. Fe particles (zero-valent Fe, Fe carbide) encapsulated in N-C shells (generically labelled as Fe@N-C) were intuitively regarded as more robust than atomically-dispersed Fe atoms (Fe-N_xC_y), due to the protective role of multi-layered graphitized N-C shell [30,47–52]. However, a more pronounced drop in ORR activity was recently reported for Fe-N-C catalysts based on Fe@N-C sites vs. those based on Fe-N_xC_y sites upon potential cycling in Ar-saturated alkaline electrolyte at 25 °C [45]. These conflicting results partly arise from the simultaneous presence of Fe-N_xC_y moieties and Fe@N-C particles in many Fe-N-C materials prepared by pyrolysis. Depending on the synthesis conditions, the carbon matrix may also feature amorphous, turbostratic or graphitic structure, [53] different porosity ranges (presence of macro and mesopores [54] or micro and mesopores [55]) and is doped with N at different rates. Such structural, textural and chemical heterogeneities prevent establishing reliable function-ORR activity-stability relationships. Moreover, the various experimental conditions used by different groups (liquid vs. solid electrolyte, potential cycling vs. constant potential, ambient temperature vs. $T \geq 60$ °C) can add to results disparities.

In this study, we investigate the stability in alkaline medium with load cycling ASTs of two Fe-N-C catalysts. Both were synthesized *via* low-energy planetary ball-milling of ZIF-8, Fe acetate and phenanthroline followed by heat treatment at 1050 °C in Ar atmosphere. However, depending on the Fe content before pyrolysis, the final materials mostly comprise Fe either as single Fe atoms or Fe carbide NPs supported onto nitrogen-doped carbon matrix, and are referred to as Fe_{0.5} and Fe_{5.0}, respectively, with the subscript number referring to the Fe weight content before pyrolysis. Their ORR activity, elemental content and distribution and carbon structure were assessed using various complementary physical, chemical and electrochemical techniques before and after AST under O₂- or Ar-saturated 0.1 mol L⁻¹ NaOH electrolyte at 60 °C or 25 °C. Our results point toward a previously undisclosed degradation mechanism into which Fe atoms dissolve and reprecipitate, and which takes place both for atomically dispersed Fe catalysts and Fe carbide NPs.

2. Experimental

2.1. Electrocatalysts

Three different Fe-N-C electrocatalysts were synthesized using zinc (II) zeolitic imidazolate framework ZIF-8 (purchased from BASF,

Basolite Z1200), iron(II) acetate, and 1,10-phenanthroline mixed *via* dry planetary ball milling in the optimized ratio, followed by pyrolysis at 1050 °C, as described in Ref. [56]. The catalysts are labelled as Fe_x, where x is the concentration of the Fe employed in the synthesis before the pyrolysis step (0, 0.5 or 5.0 wt%).

2.2. Preparation of the catalytic suspensions

To evaluate the electrocatalytic properties and the stability of the different materials, catalytic suspensions were prepared by ultrasonically dispersing 10 mg of Fe-N-C powder in a mixture of 5 wt% Nafion® solution (50 µL, Sigma-Aldrich), isopropanol (854 µL, Carl Roth) and ultrapure water (372 µL, Millipore, 18.2 MΩ cm, 1–3 ppb total organic compounds) [19]. After sonication for 15 min, aliquots of 20 µL were deposited onto a glassy carbon disc embedded into KeLF (0.196 cm² geometrical surface area), then dried using a heat gun, under controlled rotation speed resulting in a catalyst loading of 0.8 mg_{catalyst} cm⁻² for the rotating disk electrode (RDE) measurements. For the rotating ring disk electrode (RRDE) measurements, a Pt-ring and a glassy carbon disk (Pine Research) separated by a PTFE separator and a catalyst loading of 0.1 mg_{catalyst} cm⁻² were used.

2.3. Glassware cleaning and solutions

To avoid organic contamination, all glassware, electrodes, volumetric flasks and polytetrafluoroethylene (PTFE)-based materials were cleaned in 50% v/v solution of H₂SO₄ (Merck, Suprapur 96 wt%) / H₂O₂ (Carl Roth, 30% w/w) overnight followed by thorough washing and then boiling in ultrapure water (Millipore, 18.2 MΩ cm, 1–3 ppb total organic compounds) before their use. The glassy carbon discs (Sigradur® from Hochttemperatur-Werkstoffe GmbH) were polished with diamond polishing paste (1 µm, Presi). The alkaline electrolyte was prepared from NaOH (Alfa Aesar, 50% w/w aq. solution).

2.4. Electrochemical set-up

Electrochemical measurements were performed using an Autolab potentiostat (PGSTAT302N). Two different PTFE cells were used, one exclusively for the cyclic voltammograms (CVs) and ORR polarization curves at 25 °C ('characterization cell') and the other for the ASTs at 60 °C and 25 °C ('degradation cell'). A commercial RHE (Hydroflex, Gaskatel GmbH) connected to the cell *via* a Luggin capillary, and a glassy carbon plate (Sigradur® from Hochttemperatur-Werkstoffe GmbH) were used as reference electrode and counter electrode, respectively. All electrode potentials are referred to the RHE.

2.5. Electrochemical characterization and accelerated stress tests

Prior to the RDE and RRDE experiments, the electrolyte was de-aerated with argon (Ar > 99.999%, Messer). Then, 50 CVs between 0.0 and 1.0 V were performed at 100 mV s⁻¹ in Ar-purged 0.1 mol L⁻¹ NaOH ('break-in' cycles). The Ohmic drop was determined at $E = 0.10$ V using electrochemical impedance spectroscopy, and 85% of its value was dynamically compensated during the electrochemical measurements. Three CVs between 0.0 and 1.0 V at 10 mV s⁻¹ and one at 5 mV s⁻¹ were recorded in 0.1 mol L⁻¹ NaOH ('initial cycles'). The 5 mV s⁻¹ CV served to correct the ORR polarization curves from the pseudocapacitive current. The ORR activity was assessed using polarization curves at 5 mV s⁻¹ and 1600 rpm in O₂-saturated 0.1 mol L⁻¹ NaOH (O₂ > 99.99%, Messer).

The percentage of peroxide species (%HO₂⁻) and the number of electrons exchanged per O₂ molecule during the ORR (n_e) were determined using a RRDE setup (Eq. 1 and Eq. 2). During the measurement, the Pt-ring was polarized at 1.2 V vs. RHE and the electrode was rotated at 1600 rpm.

$$n_{e-} = \frac{4 |I_d|}{|I_d| + \left(\frac{I_r}{N}\right)} \quad (1)$$

$$\%HO_2^- = \frac{200 \frac{I_r}{N}}{\left(\frac{I_r}{N}\right) + |I_d|} \quad (2)$$

where I_d and I_r are the currents at the disk and ring, respectively.

The collection efficiency (N) was determined experimentally using the Fe^{3+}/Fe^{2+} redox couple from $K_3Fe(CN)_6$ salt. The experimental value was found to be $N = 0.24$.

The thin-film electrode was then transferred into the 'degradation cell', and 10,000 square-wave steps were performed between 0.6 and 1.0 V (3 s at each potential) [40]. The 0.1 mol L^{-1} NaOH electrolytes were purged with Ar or O_2 gas and kept in the controlled temperature of 60°C ; for comparison measurements were also performed at 25°C . After AST, the thin-film electrode was transferred again to the 'characterization cell' and the (break-in + initial cycles + ORR polarization curves) procedure was repeated.

The extent of degradation of the catalysts was tracked using the kinetic current densities for ORR (i_k) obtained at 1600 rpm, calculated according to the Koutecky-Levich equation. We used the O_2 diffusion-limited current density at 0.2 V and the Faradaic current obtained after pseudocapacitive current subtraction. The i_k values were then normalized by the mass (m) of catalyst deposited onto the glassy carbon disk, and expressed as MA.

2.6. Transmission electron microscopy (TEM), scanning transmission electron microscopy (STEM) and energy-dispersive X-ray spectroscopy (X-EDS)

A JEOL 2010 TEM instrument operated at 200 kV with a point-to-point resolution of 0.19 nm was used for TEM imaging. X-EDS spectra were obtained in at least 6 different regions of the TEM grid. The quantification analysis was performed on the Fe K lines, using the K -factor provided by the JEOL software. The mean nanoparticle size and nanoparticle density were determined using the software *ImageJ*.

The STEM/X-EDS elemental maps were acquired using a JEOL 2100 F microscope operated at 200 kV equipped with a retractable large angle Centurio Silicon Drift Detector (SDD) detector. We used the Fe K , C K and O K lines and the K -factors provided by the JEOL software.

2.7. X-ray photoelectron spectroscopy (XPS)

XPS data were obtained on a Thermo Scientific K_α spectrometer using a monochromated Al X-ray source ($h\nu = 1486.6 \text{ eV}$ and spot size $400 \mu\text{m}$). They were measured directly onto the thin-film electrodes before/after ageing. The XPS spectra of O1s, N1s and C1s were fitted using CasaXPS software to obtain the surface composition of the catalysts. Binding energies were corrected to the reference of the C-C component of C1s (sp^2 and sp^3 -hybridized carbon atoms) peak at 284.3 eV .

2.8. Raman spectroscopy

The Raman spectra were recorded on a Renishaw inVia Raman system, with an excitation wavelength at 532 nm . Measurements were performed in a backscattering configuration, using a $50\times$ microscope objective, and a $2400 \text{ grooves mm}^{-1}$ grating. This configuration ensured a spectra resolution much better than 1 cm^{-1} . To decrease the incident power at the sample, the line mode of the spectrometer was used. This configuration allowed to record 'averaged' spectra over an area of ca. $50 \mu\text{m}^2$ in a single shot, with a power density at the sample much less than $50 \mu\text{W } \mu\text{m}^{-2}$. For visualization purposes, the spectra were simply normalized to the amplitude of the 'G' mode, located at 1580 cm^{-1} .

2.9. Inductively coupled plasma-mass-spectrometry (ICP-MS)

The amount of Fe dissolved in the electrolyte was determined using a PerkinElmer NexION 2000 ICP-MS. The Fe calibration curve was obtained from standard monometallic solution (Iron ICP Standard Solution, 1000 mg L^{-1} , Carl Roth GmbH & Co. KG), diluted with a 0.05 mol L^{-1} NaOH solution to obtain analytical metal concentrations of 2, 5, 10, and $20 \mu\text{g L}^{-1}$. The collected electrolyte was diluted twice to decrease the aliquot's pH, and bring the analyte concentrations into the specified calibration ranges. Rhodium (Rh) was used as internal standard due to its similar first ionization energy compared to Fe (7.5 and 7.9 keV , respectively). Sample and calibration solutions were spiked with a $2.5 \mu\text{g L}^{-1}$ of ^{103}Rh internal standard solution (PerkinElmer). To attenuate polyatomic interferences (e.g. ^{40}Ar and ^{16}O), we analysed ^{56}Fe and used the helium collision mode with kinetic energy discrimination.

2.10. X-ray absorption spectroscopy (XAS) and X-ray emission (XES) spectroscopy

High energy-resolution fluorescence-detected X-ray absorption near edge structure (HERFD-XANES) and $K\beta$ XES spectra were recorded at beamline ID26 at the European Synchrotron Radiation Facility (ESRF), Grenoble, France. Si (111) double-crystal monochromator was used for the measurements. The maximum of Fe $K\beta$ fluorescence line (7.058 keV) was selected with an emission spectrometer in Rowland geometry with five Ge (620) analyser crystals (Bragg angle, 79°). The incident beam absolute energy calibration was performed using a reference metallic Fe foil by setting the first inflection point of the Fe K edge at 7.112 keV . The incident energy was varied from 7.10 to 7.20 keV over Fe K edge. HERFD-XANES spectra were recorded in continuous mode during 5 min with an energy step of 0.1 eV . The XES spectra were collected with a step size of 0.1 eV and an incident energy of 7.80 keV . The measurements were performed on glassy carbon-based electrodes, using a catalyst loading of $0.8 \text{ mg}_{\text{catalyst}} \text{ cm}^{-2}$. The analyses were performed before and after ASTs, at room temperature and in the presence of air. HERFD-XANES and XES spectra were normalized in area using the ranges $7.10 - 7.20 \text{ keV}$ and $7.02 - 7.07 \text{ keV}$, respectively. Several scans were averaged.

2.11. Wide-angle X-ray scattering measurements (WAXS) and pair distribution function (PDF) analysis

The WAXS measurements were performed at ID31 beamline of the ESRF in Grenoble, France. Radiation from one undulator was monochromatized with a multilayer monochromator (bandwidth 2%) to the final energy of 70 keV ($\lambda = 0.177 \text{ \AA}$). Sample powders were measured in Kapton capillaries of 1 mm in diameter and the scattered signal was collected using a Dectris Pilatus CdTe 2 M detector. The energy, detector distance and tilts were calibrated using a standard CeO_2 powder and the 2D diffraction patterns were reduced to 1D curves using the pyFAI software package [57].

The PDF patterns were calculated using the PDFGetX2 software [58]. After subtraction of the environment contribution using an empty capillary measurement and corrections for absorption and inelastic scattering, the data were normalized and Fourier transformed using $Q_{\text{max}} = 19.3 \text{ \AA}^{-1}$. In order to calculate the difference-PDF patterns, the PDFs from the 3 samples were normalized by using the intensity of the first peak at 1.4 \AA , to which Fe atoms are not expected to contribute due to the too short distance. The difference-PDF patterns will thus contain the contributions of atomic pairs containing at least one Fe atom.

3. Results

3.1. Structural and chemical properties of the fresh and aged Fe-N-C electrocatalysts

The catalysts studied in this work have been extensively characterized by XAS, Raman spectroscopy, ^{57}Fe Mössbauer spectroscopy, TEM, X-EDS, X-ray diffraction and Brunauer-Emmett-Teller (BET) techniques in our former works [19,25,56,59,60]. In brief, TEM images showed the absence of Fe particles in the $\text{Fe}_{0.5}$ catalyst and this was confirmed by the absence of a peak at $ca. 2.1\text{--}2.2 \text{ \AA}$ in the Fourier transform of its EXAFS spectrum and also by the absence of a sextet component in its ^{57}Fe Mössbauer spectrum [19,25,61]. In contrast, the same characterizations performed on $\text{Fe}_{5.0}$ revealed only or mostly Fe carbide NPs [19]. These conclusions are supported by Fig. 1 showing the PDF analyses of the WAXS patterns for $\text{Fe}_{0.5}$ and $\text{Fe}_{5.0}$ and for a catalyst synthesized in the exact same manner as $\text{Fe}_{0.5}$ and $\text{Fe}_{5.0}$ but in the absence of Fe ($\text{Fe}_{0.0}$). Indeed, after normalization to the intensity of the C-C peak at $ca. 1.41 \text{ \AA}$, [62] the 'Normalized $\text{Fe}_x\text{-Fe}_{0.0}$ ' traces allow to directly visualize the structure of the minority compounds, once the signal of the carbon matrix is cancelled.

Intense bands at 2.60, 3.77, 4.23, 4.57 and 5.19 angströms are observed in the 'Normalized $\text{Fe}_{5.0}\text{-Fe}_{0.0}$ ' difference signal, in close agreement with the PDF calculated using the Fe_3C structure. This result is in line with former XAS, XRD and ^{57}Fe Mössbauer spectroscopy results, which evidenced the presence of Fe_3C NPs in $\text{Fe}_{5.0}$ [19]. The Fe content after the pyrolysis step is close to 15 wt%, and the structure of the carbon matrix is highly graphitic leading to a BET specific surface area $ca. 450.0 \text{ m}^2 \text{ g}^{-1}$.

In contrast, for the $\text{Fe}_{0.5}$ catalyst, we noticed no bonds typical of Fe-Fe and Fe-C bands in the 'Normalized $\text{Fe}_{0.5}\text{-Fe}_{0.0}$ ' difference signal, providing evidence of the absence of Fe-based NPs, at least within the detection limit of the WAXS technique. The Fe content in this catalyst was measured to be $ca. 1.3 \text{ wt\%}$ after pyrolysis, and its BET specific surface area approaches $700.0 \text{ m}^2 \text{ g}^{-1}$ due to the simultaneous presence of mesopores and micropores. Finally, XPS measurements indicate high content of pyrrolic and pyridinic N species in both $\text{Fe}_{0.5}$ and $\text{Fe}_{5.0}$ catalysts (Fig. S1).

Fig. 2 displays TEM, STEM images and STEM/X-EDS elemental maps of the $\text{Fe}_{0.5}$ catalyst before (Fig. 2a-d) and after an AST composed of 10,000 square cycles between 0.6 and 1.0 V (3 s at each potential) in oxygen (O_2)-saturated 0.1 mol L^{-1} NaOH electrolyte at 25°C (Fig. 2e-h) or 60°C (Fig. 2i-l). For the ease of reading, we refer to the ASTs as: [low potential – high potential – duration of each potential step – number of cycles – nature of the atmosphere – temperature] in what follows. TEM (Fig. 2a) and STEM (Fig. 2b) images, and STEM/X-EDS elemental maps (Fig. 2c and Fig. 2d) confirm that Fe atoms are homogeneously

distributed in the fresh $\text{Fe}_{0.5}$ material, and that it was free of Fe NPs. Pronounced morphological changes are observed upon ageing: the aged $\text{Fe}_{0.5}$ catalyst exhibits NPs, whose size approaches 20–30 nm after $[0.6\text{--}1.0 \text{ V} - 3 \text{ s/3 s} - 10 \text{ k} - \text{O}_2 - 25^\circ\text{C}]$ (Fig. 2e-h) and $< 10 \text{ nm}$ after $[0.6\text{--}1.0 \text{ V} - 3 \text{ s/3 s} - 10 \text{ k} - \text{O}_2 - 60^\circ\text{C}]$ (Fig. 2i-l), as quantitatively shown by the particle size distributions of Fig. S2. The formation of NPs was also observed when argon (Ar) was used to saturate the electrolyte (Fig. S3 and Table S1). This experiment suggests that the morphological changes are controlled by the electrode potential, not by the gas atmosphere. Interestingly, not only does the morphology of the Fe-N-C catalyst change after AST, but also its chemical composition. Indeed, point X-EDS analyses performed at several particles of the aged $\text{Fe}_{0.5}$ catalyst indicated an oxygen:iron (O:Fe) stoichiometry of 3.1 ± 0.3 and 2.5 ± 0.5 after AST at 25 and 60°C , respectively.

Similarities but also pronounced differences were observed for the $\text{Fe}_{5.0}$ catalyst (Fig. 3). Fe-rich particles with sizes of 5–30 nm are seen in the fresh sample (Fig. 3a-b), while O atoms homogeneously cover the surface of the carbon matrix (adventitious oxygen and oxygen groups on carbon matrix), with no evidence, initially, for increased O signal at the Fe-rich particles (Fig. 3c and Fig. 3d). However, a distinct core@shell structure composed of a Fe-rich core covered by a Fe-poor and O-rich shell (Fig. 3g-h) is observed for some of the NPs after the $[0.6\text{--}1.0 \text{ V} - 3 \text{ s/3 s} - 10 \text{ k} - \text{O}_2 - 60^\circ\text{C}]$ protocol. This core@shell structure is confirmed by the point X-EDS analyses performed in the core or the shell region of the NP (Fig. S4a), the colour map composition (Fig. S4b) and the line-scan profiles displayed in Fig. S4c-d. Combined with the marked increase of the mean particle size from 17 nm to 36 nm in the particle size distribution histograms (Fig. S2) and the drop in the NP density (Table S1), the results suggest that Fe atoms redistributed during the AST, as a result of a Fe dissolution/Fe oxide reprecipitation mechanism. This result is in line with what we have reported previously in acidic electrolyte, [20,61] and with recent IL-TEM images and XAS results from García *et al.* [52] showing that Fe oxide NPs form during ageing in alkaline electrolyte of a Fe-N-C catalyst initially comprising a mix of Fe_3C particles and $\text{Fe-N}_x\text{C}_y$ sites. Some other Fe-based NPs are however free of an O-rich shell after AST, and this may be explained by the perfect encapsulation of these Fe_3C NPs by a graphite shell in the fresh $\text{Fe}_{5.0}$ catalyst (Fig. 3g, particle on top).

To investigate changes in the electronic structure of Fe atoms during ageing in 0.1 mol L^{-1} NaOH, we performed HERFD-XANES and XES on the $\text{Fe}_{0.5}$ catalyst before and after the $[0.6\text{--}1.0 \text{ V} - 3 \text{ s/3 s} - 10 \text{ k} - \text{Ar} - 60^\circ\text{C}]$ and $[0.6\text{--}1.0 \text{ V} - 3 \text{ s/3 s} - 10 \text{ k} - \text{O}_2 - 60^\circ\text{C}]$ protocols. The Fe K edge spectra (Fig. 4a) can be divided into two regions based on the electronic transitions that give rise to the spectral features: the rising absorption edge or the white line ($1s \rightarrow 4p$ transition) and the pre-edge ($1s \rightarrow 3d$ transition), the latter being displayed in the inset of Fig. 4a. One can clearly observe a shift of the edge position in the aged $\text{Fe}_{0.5}$

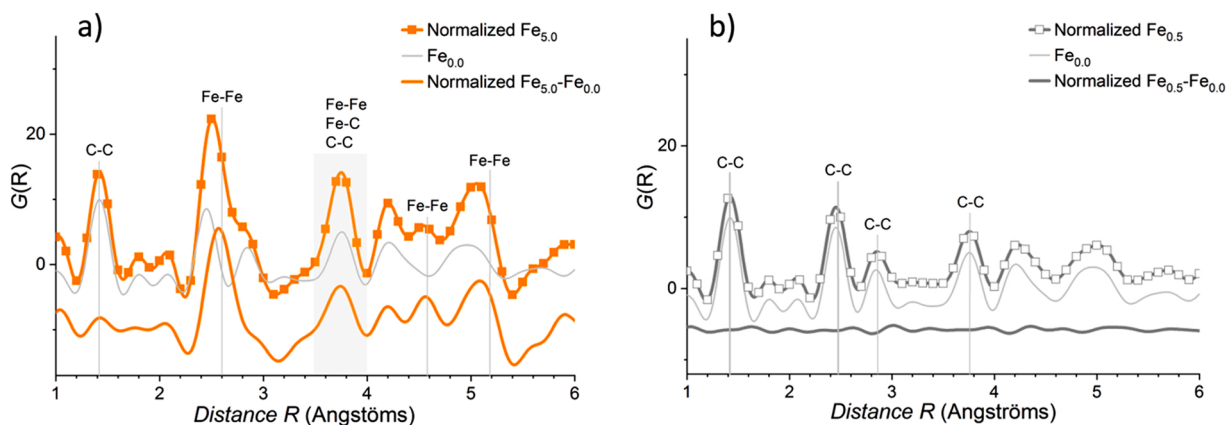


Fig. 1. Structural characterisation of the fresh (a) $\text{Fe}_{5.0}$ and (b) $\text{Fe}_{0.5}$ catalysts. The graphs include the normalized and the $\text{Fe}_{0.0}$ -subtracted-pair distribution function analyses of the wide-angle X-ray scattering patterns.

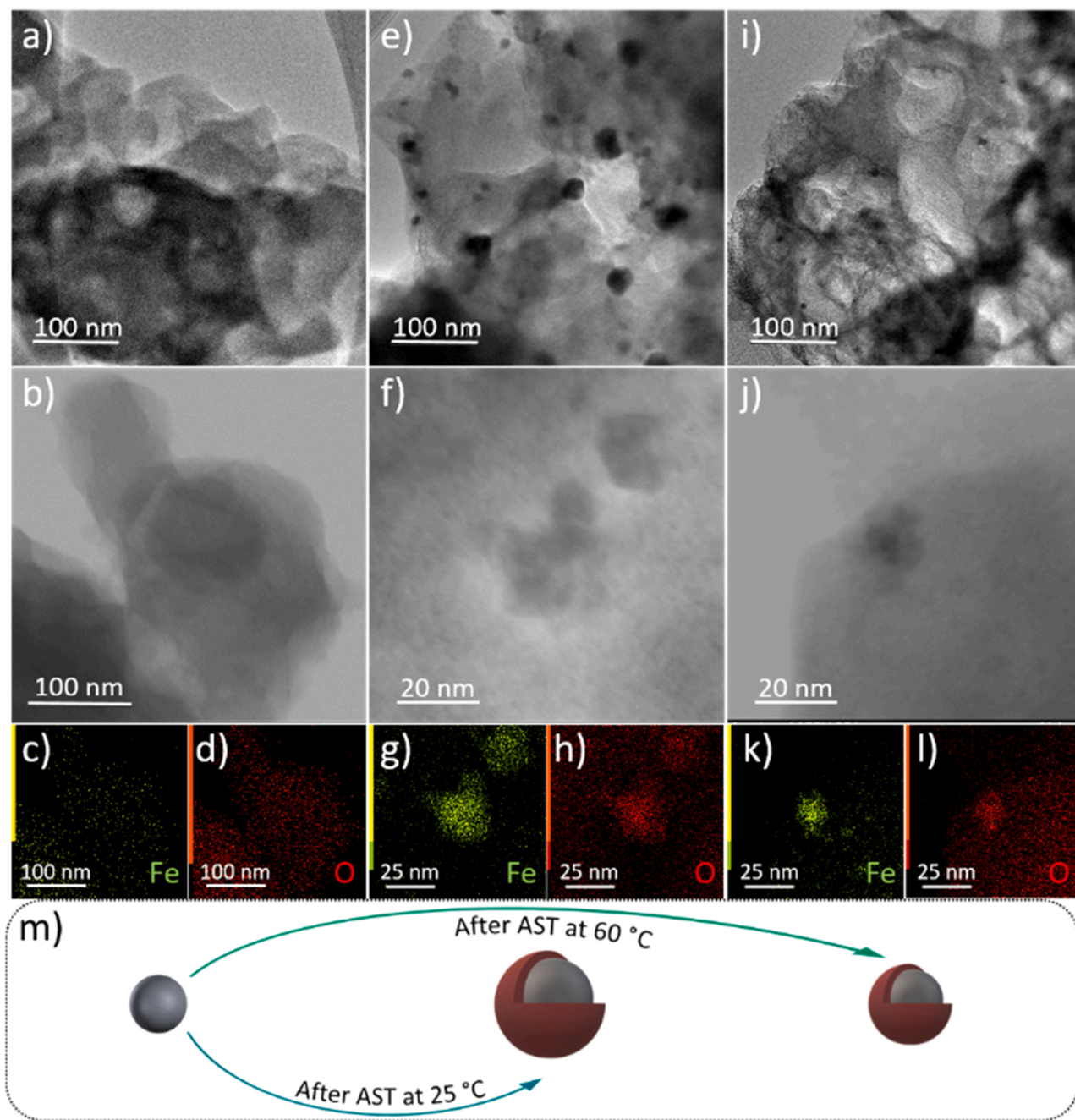


Fig. 2. Morphological and chemical characterisation of the fresh and aged $\text{Fe}_{0.5}$ catalysts. TEM images, STEM images and associated X-EDS elemental maps of $\text{Fe}_{0.5}$ (a-d) before and after 10,000 square cycles between 0.6 and 1.0 V (3 s at each potential) in O_2 -saturated 0.1 mol L^{-1} NaOH at (e-h) 25°C and (i-l) 60°C . (m) Illustration of the proposed mechanism of the partial transformation of a restricted number of initially-surface-exposed $\text{Fe-N}_x\text{C}_y$ moieties into FeO_x nanoparticles and of its temperature-dependence. The elemental maps are built from Fe K and O K lines, Fe and O atoms are represented in green and red, respectively.

sample that can be assigned either to an increase in the average oxidation state of Fe atoms and/or to changes in the local geometry of Fe sites [63]. The analysis of the pre-edge features (Fig. 4a, inset) also shows significant changes in the peak intensities after the ASTs. The assignment of these peaks to specific structures is not-trivial due to the intrinsic complexity of these materials' composition. However, based on the observed changes, one may assume one or several of the following phenomena took place: (i) distortion of $\text{Fe-N}_x\text{C}_y$ sites; (ii) transformation of certain $\text{Fe-N}_x\text{C}_y$ sites into ferric oxide upon ageing.

We also measured $K\beta$ XES spectra on the fresh and aged $\text{Fe}_{0.5}$ catalysts (Fig. 4b). This method is traditionally used for spin-state studies [64,65] as the shape of the $K\beta$ line is dominated by the $3p - 3d$ exchange

interaction. This emission line comprises two features: high-energy $K\beta_{1,3}$ and low-energy $K\beta'$, where the intensity of the latter and the energy separation between these two peaks are spin sensitive. [64] The increase of the $K\beta'$ shoulder observed in the aged samples (inset of Fig. 4b) as well as the increased energy split between the features in comparison to a fresh sample evidence higher average spin state of Fe in the aged $\text{Fe}_{0.5}$ catalyst. The increase of the spin state is directly correlated to the local geometry changes, e.g. due to oxidation of Fe atoms or to the formation of other structures, such as Fe oxide NPs. Moreover, the changes in HERFD-XANES and XES spectra discussed above are independent of the gas atmosphere used during the AST, which confirms the STEM/X-EDS analyses (Fig. 2, 3 and Fig. S4).

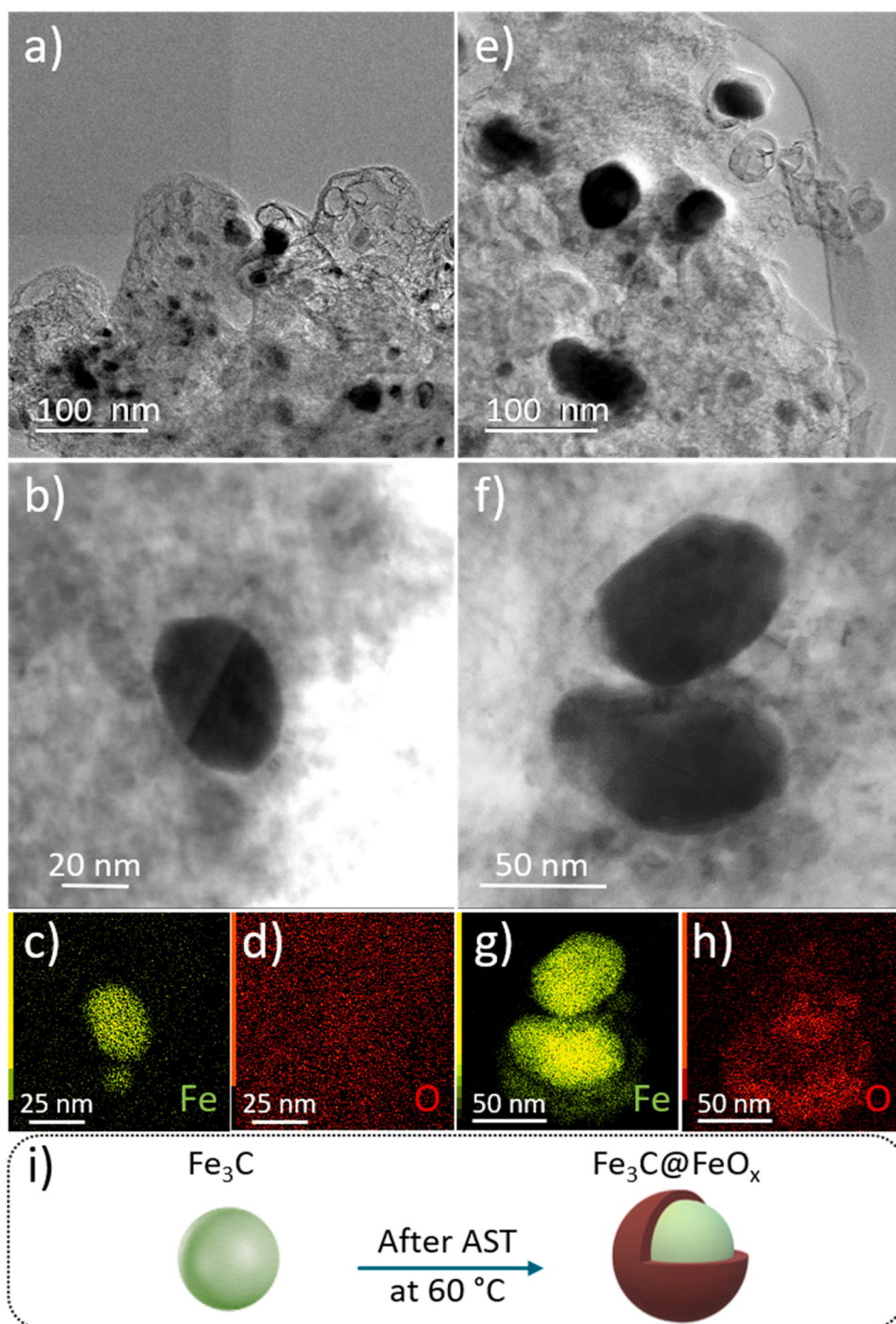


Fig. 3. Morphological and chemical characterisation of the fresh and aged $\text{Fe}_{5.0}$ catalysts. Representative TEM images, STEM images and associated X-EDS elemental maps of $\text{Fe}_{5.0}$ catalyst (a-d) before and (e-h) after 10,000 cycles between 0.6 and 1.0 V (3 s at each potential) in O_2 -saturated 0.1 mol L^{-1} NaOH at 60°C . (i) Illustration of the proposed mechanism of the transformation of electrolyte-accessible Fe_3C into $\text{Fe}_3\text{C}@\text{FeO}_x$ core-shell structure. The elemental maps are built from Fe *K* and O *K* lines, Fe and O atoms are represented in green and red, respectively.

3.2. Fe redistribution at the electrode | electrolyte interface

At this point, it is however still unclear whether the transformation process of some single Fe atoms or some Fe_3C NPs into Fe oxides occurs via (i) de-coordination of $\text{Fe}^{2+}/\text{Fe}^{3+}$ ions from N atoms, mobility on the carbon surface and aggregation upon collision (applicable not only for Fe_3C particles, but also to $\text{Fe-N}_x\text{C}_y$ sites, as recently observed in Ref. [66]) or (ii) passage of $\text{Fe}^{2+}/\text{Fe}^{3+}$ ions in the electrolyte and then re-precipitation as Fe oxides. To answer this question, the percentage of Fe dissolved in electrolyte was calculated by assessing the increase in Fe concentration in the electrolyte during AST normalized to the maximal Fe concentration achievable based on the Fe content in the fresh thin-film electrode (Fig. S5a). The results show that ca. 15% of the Fe

atoms was dissolved in the electrolyte after either [0.6–1.0 V – 3 s/3 s – 10 k – Ar – 60°C] or [0.6–1.0 V – 3 s/3 s – 10 k – O_2 – 60°C] for the $\text{Fe}_{0.5}$ sample, while only ca 3% of all Fe atoms was dissolved for $\text{Fe}_{5.0}$ during the same AST protocols. The similar Fe leaching observed in Ar- or O_2 -saturated NaOH electrolyte (for a given Fe-N-C catalyst) confirms the conclusions derived from HERFD-XANES (Fig. 4) and TEM/STEM (Fig. 2, Fig. 3 and Fig. S4) that the gas atmosphere plays a minor role in the degradation mechanism/kinetics of Fe-N-C materials in alkaline medium, at least in the potential range investigated in our study. It is also interesting to relate the 15% number for $\text{Fe}_{0.5}$ to the 'utilization factor' of Fe as Fe-N_4 sites in the pristine $\text{Fe}_{0.5}$ catalyst, i.e. to the fraction of electrochemically-accessible Fe sites. An utilization factor of 22% was found by Bae *et al.* for the $\text{Fe}_{0.5}$ pristine catalyst used in our study [67].

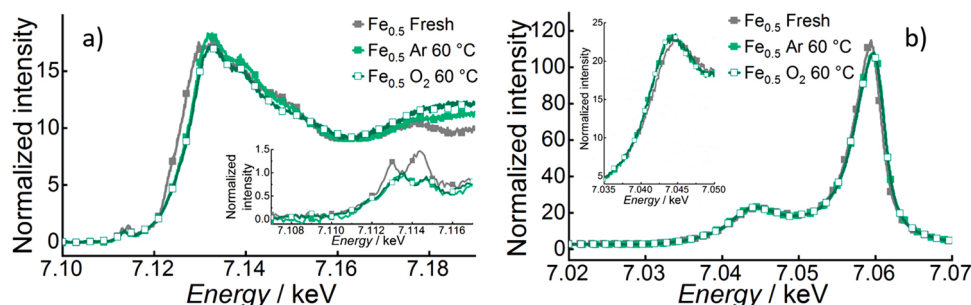


Fig. 4. (a) $K\beta$ – detected Fe K edge HERFD XANES and (b) Fe $K\beta$ XES spectra of fresh and aged $Fe_{0.5}$ catalyst. The spectra are normalized by the incoming flux and by the area under the curve, hence ‘Normalized intensity’ translates into ‘Area-normalized intensity’. The insets of panels a and b show a zoom in the pre-edge and $K\beta$ regions, correspondingly.

Thus, 15% of Fe atoms (relative to the bulk Fe content) dissolved after the ASTs (either [0.6–1.0 V – 3 s/3 s – 10 k – Ar – 60 °C] or [0.6–1.0 V – 3 s/3 s – 10 k – O_2 – 60 °C], Fig. S5a) implies that $15/22 \times 100 = 68\%$ of all the $Fe-N_4$ sites situated on the surface initially has been leached in the electrolyte.

Complementary to ICP-MS analyses of the electrolyte, the residual Fe content within the aged thin-film electrodes was also analysed using X-EDS, and is expressed as the ratio of the Fe content in the Fe-N-C thin-film electrode before and after different ASTs ([final Fe at%] / [fresh Fe at%]) in Fig. S5b. For $Fe_{0.5}$, the X-EDS analyses were performed in multiple areas of regions free of Fe NPs, in order to assess the density of intact $Fe-N_xC_y$ moieties. In contrast, they were performed randomly on the surface of the pristine/aged $Fe_{5.0}$ catalyst since NPs are present at any stage of ageing. The X-EDS results show that: (i) the Fe losses were comparable after AST under Ar- and O_2 -saturated electrolyte, (ii) the Fe content decreased by ca. 20% in the $Fe_{5.0}$ catalyst after [0.6–1.0 V – 3 s/3 s – 10 k – O_2 – 60 °C], (iii) and by ca. 50% for $Fe_{0.5}$ after the same AST, and (iv) there was almost no decrease of the Fe content for $Fe_{0.5}$ after the same AST but at 25 °C (Fig. S5b). Together with the electrolyte’s analyses and material’s characterisation, the results indicate that ca. 50% of the $Fe-N_xC_y$ moieties in $Fe_{0.5}$ were destroyed after [0.6–1.0 V – 3 s/3 s – 10 k – O_2 – 60 °C], and that Fe-oxide NPs formed by reprecipitation. For $Fe_{5.0}$, the lower decrease of Fe content during the same AST indicates that most of the leached Fe atoms reprecipitated quickly inside the thin-film electrode in the form of Fe-oxides. Although surprising at first sight, these results simply translate the dependence of the Nernst potential on the local concentration of Fe in the electrolyte filling the porosity of the thin-film during the AST. Indeed, due to higher initial Fe content in the thin-film electrode for $Fe_{5.0}$ vs. $Fe_{0.5}$, higher Fe concentrations in the Helmholtz plane are expected for the former during the AST, and these favour the precipitation of a Fe oxide shell on top of Fe_3C NPs.

These results are important for the practical application of various Fe-N-C materials with different Fe speciation in AEMFCs and metal-air batteries. For $Fe_{0.5}$, they are in good qualitative agreement with the reported decrease of the amount of $Fe-N_xC_y$ sites and the concomitant increase of Fe-oxides, as observed by ^{57}Fe Mössbauer spectroscopy on another Fe-N-C material based on single-atom-sites, before/after a 100 h durability test at 600 mA cm^{-2} in air/ H_2 AEMFC [68]. We also stress that while the reprecipitation of Fe as Fe oxide during AST was quantitatively limited for $Fe_{0.5}$ in liquid alkaline electrolyte, the outcome in an ionomeric environment free of support liquid electrolyte (stronger increase in local Fe concentration in the ionomer phase) is expected to favour the reprecipitation of leached Fe cations as Fe oxide [61].

The question now arises whether the release of Fe cations in the electrolyte was caused or simply accelerated by the corrosion of the carbon matrix. Raman spectroscopy and X-ray photoelectron spectroscopy are ideal tools to provide answers to this question. The Raman spectra of the Fe-N-C catalysts before and after ageing at 60 °C are shown in Fig. S6. They are dominated by the defect and/or disorder-induced $D1$ -band at $\nu \sim 1350\text{ cm}^{-1}$ and $D2$ band at $\nu \sim 1610\text{ cm}^{-1}$ and

the Raman-allowed graphitic G band at $\nu \sim 1580\text{ cm}^{-1}$, thus signing the presence of disordered and ordered domains, respectively [69]. Second-order Raman bands at $\nu \sim 2690, 2950$ and 3190 cm^{-1} were also observed, mostly due to the combination and overtones of $D1$ and G bands. Again, the second-order regions of the spectra were ill-defined, translating structural disorder within the materials [70]. In more details, a slight decrease in the intensity of the $D1$ - and $D2$ -bands relatively to the G -band intensity was observed on the $Fe_{0.5}$ catalyst after all ASTs, suggesting preferential corrosion of the most defective regions of the carbon matrix. As such domains may correspond to the microporous carbon regions, hosting some of the $Fe-N_xC_y$ sites in MOF-derived catalysts, the results are in line with the drop of the Fe content monitored by X-EDS analyses (performed on NP-free areas of the $Fe_{0.5}$ catalyst, Fig. S5a). In contrast, for the more graphitic $Fe_{5.0}$ catalyst, the intensity of the $D1$ - and $D2$ -bands slightly increased, suggesting the formation of point in-plane defects or a small decrease of the mean in-plane coherent domain size. Note that similar experimental trends were observed on Pt/high-surface-area carbon (Ketjenblack type) and Pt/reinforced graphite NPs by Castanheira et al. [22,23].

Because surface defects of carbon materials are quickly populated by oxygen-containing groups in aqueous electrolyte, [71] structural changes in the carbon matrix should also lead to chemical changes. Fig. S1a shows the deconvoluted $O1s$, $N1s$ and $C1s$ regions of the XPS spectra of the $Fe_{0.5}$ and $Fe_{5.0}$ electrocatalysts before/after [0.6–1.0 V – 3 s/3 s – 10 k – Ar – 60 °C], and the atomic percentages of the different chemical groups are displayed in Table S2. It can be observed that O atoms contained in the pristine Fe-N-C catalysts mostly participate in C-O-H/C-O-C bonds. However, the balance between the different groups changes upon ageing, C-O-H groups being progressively converted/oxidized into C=O groups (Eq. 3):



These findings are in line with the $N1s$ region of the XPS spectra. Indeed, the distribution of N species was mostly unchanged upon ageing (see Table S2); however, the fraction of oxidized N raised at the expense of pyrrolic N for the more graphitized Fe-N-C catalyst ($Fe_{5.0}$). This is in line with former literature reports pointing towards the instability of pyrrolic N [52] and the stability of graphitic N in alkaline electrolyte [72]. Finally, as evidenced by the bar chart in Fig. S1c, the C-C functional group was predominant for the fresh and aged $Fe_{0.5}$ and $Fe_{5.0}$ catalysts, and its intensity mildly varied, corroborating the conclusions derived from Raman spectroscopy (Fig. S6).

Summing up, Raman spectroscopy and XPS results suggest that corrosion of the N-C matrix was mild in alkaline electrolyte, and mostly proceeded on the surface and near-surface region of the Fe-N-C catalysts.

3.3. Electrocatalytic properties of fresh and aged Metal-N-C electrocatalysts

Fig. 5a-e displays Ohmic-drop corrected CVs obtained before and

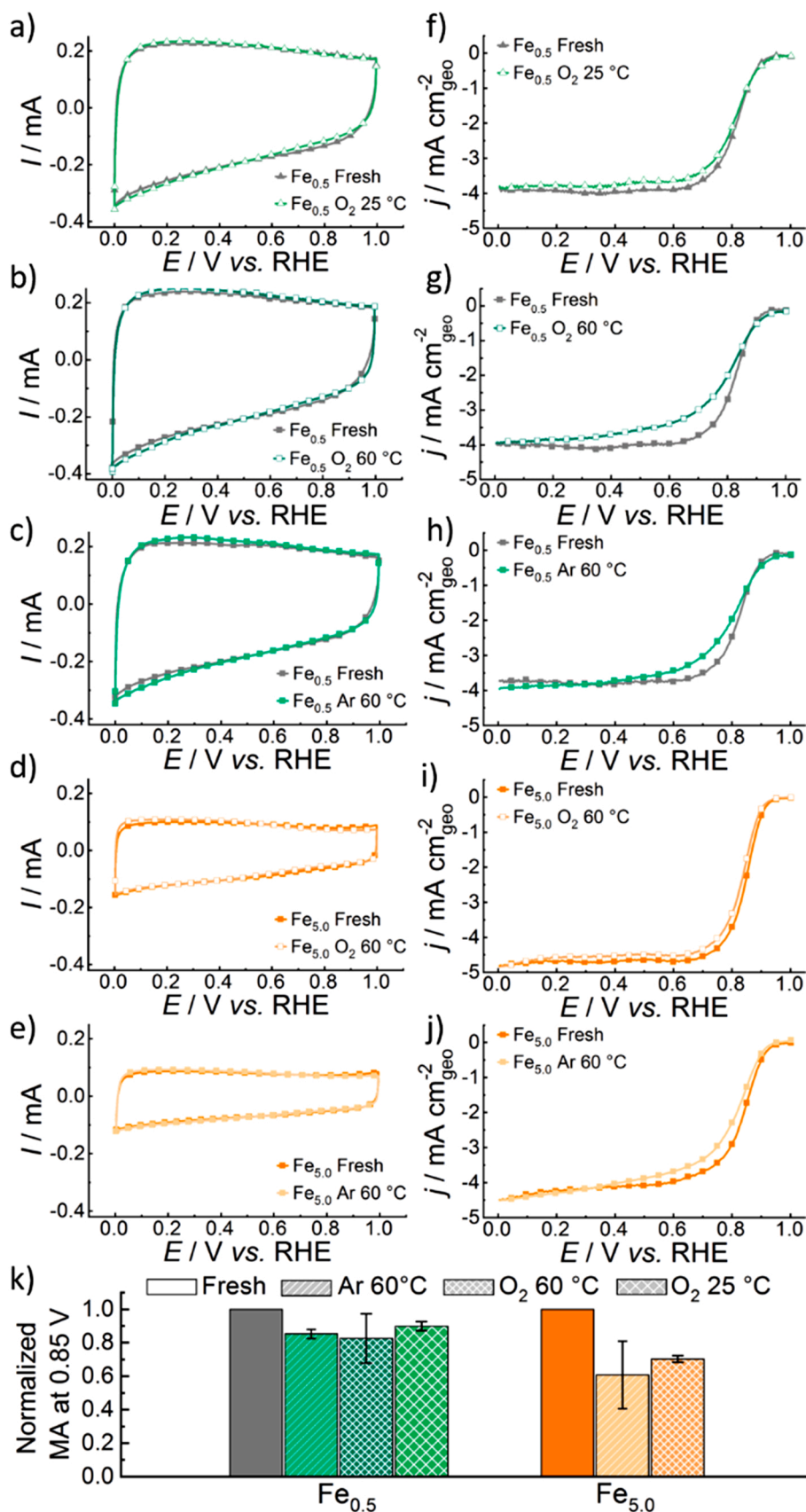


Fig. 5. Cyclic voltammograms of (a, b, c) $\text{Fe}_{0.5}$ and (d, e) $\text{Fe}_{5.0}$ electrocatalysts and ORR polarization curves of (f, g, h) $\text{Fe}_{0.5}$ and (i, j) $\text{Fe}_{5.0}$ measured before and after 10,000 load-cycles in Ar- or O_2 -saturated 0.1 mol L^{-1} NaOH electrolyte at 25 °C or 60 °C. (k) Normalized MA towards the ORR measured at $E = 0.85 \text{ V}$ for the pristine/aged catalysts. Cyclic voltammograms were performed in Ar-purged 0.1 mol L^{-1} NaOH at a scan rate of 10 mV s^{-1} using a catalyst loading of $0.8 \text{ mg}_{\text{catalyst}} \text{ cm}^{-2}$ and a temperature of 25 °C. The ORR polarization curves were recorded using a catalyst loading of $0.8 \text{ mg}_{\text{catalyst}} \text{ cm}^{-2}$ (potential scan rate 5 mV s^{-1} , $T = 25 \text{ °C}$ and $w = 1600 \text{ rpm}$).

after [0.6–1.0 V – 3 s/3 s – 10 k – O₂ – 60 °C], [0.6–1.0 V – 3 s/3 s – 10 k – Ar – 60 °C] or [0.6–1.0 V – 3 s/3 s – 10 k – O₂ – 25 °C]. The CVs indicated that the N-C matrix of both catalysts did not suffer severe physical and chemical degradations during the ASTs, in agreement with the conclusions derived from XPS and Raman spectroscopies. Indeed, similar pseudocapacitive currents were observed in the CV of the Fe_{0.5} and the Fe_{5.0} catalysts before and after ageing in Ar- or O₂-saturated 0.1 mol L⁻¹ NaOH at 60 °C, as expected from mild functionalization with oxygen-containing surface groups [19,25]. The ORR polarization curves recorded on the fresh and aged Fe-N-C catalysts are shown in Fig. 5f-j. They display regions where the ORR kinetics is under pure activation control ($E > 0.85$ V), under mixed activation-O₂ diffusion control ($0.6 < E < 0.85$ V) and under control by O₂ diffusion in solution ($E < 0.6$ V). We note that the MA towards the ORR of Fe_{0.5} decreased by only ca. 10–20% at $E = 0.85$ V during ageing (Fig. 5k), but by a higher amount of ca. 45% at $E = 0.80$ V (Table S3). A detailed analysis shows that the Tafel slope of Fe_{0.5} was significantly increased after AST (Fig. S7), explaining the dependence of the % loss of MA with the potential chosen to report the MA. These numbers can be compared to the relative amount of Fe-N_xC_y moieties lost during AST, which were estimated by X-EDS and ICP-MS results to be in the range of 50–68%. The results are similar in the O₂ diffusion-limited region of the ORR polarization curve, where the initial current density dropped by less than 10% upon ageing at 60 °C (Fig. 5 g-h), which suggests unmodified selectivity upon AST. The RRDE results displayed in Fig. S8 and S9 and Table S4 quantitatively confirm this trend. For Fe_{5.0}, the ORR activity at $E = 0.85$ V decreased more markedly by ca. 30–40% after the different ASTs (Fig. 5k), while the Tafel slope was unmodified in this case (Table S3). In contrast, there was no significant change of the current density in the O₂ diffusion-limited region (Fig. 5 i-j).

4. Discussion

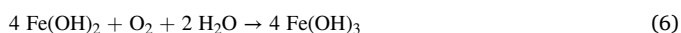
We now discuss all the results of physico-chemical and electrochemical characterizations to draw conclusions on the transformation process of different Fe-N-C catalysts into Fe oxides in alkaline electrolyte, and its impact on the final ORR activity.

Our findings firstly point towards the absence of massive ORR-assisted carbon corrosion in alkaline compared to acidic electrolyte. Indeed, in acidic electrolyte, Fenton reactions between Fe atoms and H₂O₂ molecules formed as ORR intermediates catalyse the formation of radical species (*OH, *OOH). These radical species then irreversibly oxidize the carbon matrix, ultimately leading to the demetallation of the Fe-N_xC_y moieties [20]. The results reported in this work illustrate similar, although much less pronounced, changes in morphology and chemistry during ORR in alkaline electrolyte. They suggest that the superoxide anion O₂⁻ radical species formed at pH > 12 is less reactive than *OH and *OOH species, in line with the former report of Bae et al. [73]. The Fe-N-C catalysts based on zero-valent Fe NPs are also prone to dissolution and transformation into Fe oxide, if they are initially accessible by the electrolyte, or as a result of their exposure to the electrolyte due to mild carbon corrosion during the AST.

The dissolved Fe²⁺ and Fe³⁺ cations are then prone to reprecipitate as Fe(OH)₂ and Fe(OH)₃, in agreement to what was observed in 0.1 M H₂SO₄ and in PEMFC in our former studies: [20,61]



Note that any deposited Fe(OH)₂ species will spontaneously transform into Fe(OH)₃, due to the presence of O₂ and/or due to the one order of magnitude lower solubility constant of Fe(OH)₃ over Fe(OH)₂: [74]



The local STEM/X-EDS analyses support this assertion, as the

average ratio between O and Fe atoms (calculated from at least 3 different STEM images) was 3.1 ± 0.3 and 2.5 ± 0.5 for Fe_{0.5} after AST at 25 °C or 60 °C, respectively.

Importantly, the ORR proceeding at single Fe atoms or Fe₃C NPs leads to the formation of OH⁻ ions, and to a more basic environment in the Helmholtz plane that facilitates the rapid complexation of the free Fe²⁺/Fe³⁺ ions (see the larger size and higher density of NPs after ageing in O₂- vs. Ar-saturated electrolyte in Table S1, respectively). Once formed, Fe(OH)₂ and Fe(OH)₃ species are in equilibrium with HFeO₂⁻/Fe₂O⁻ and FeO₂⁻/HFeO₃²⁻/FeO₃³⁻ species in alkaline solution [75]. However, the small solubility constants of Fe hydroxides in high pH electrolyte (close to 10⁻⁶ and 10⁻⁷ for Fe(OH)₂ and Fe(OH)₃, [74] respectively) thermodynamically favour the solid products.

The effect of temperature is also worth being discussed. Firstly, the carbon matrix corrodes faster when the temperature increases [76]. Besides, in the frame of Le Chatelier principle, the equilibrium between the solid metal oxides and the dissolved Fe²⁺/Fe³⁺ species will be displaced to counteract any change in temperature. Since the enthalpy of formation of Fe oxides is exothermic, [75] the equilibrium will be displaced to favour their dissolution when the temperature of the AST increases. More pronounced losses of Fe, larger variations of the mean NP size and of the NP density for the Fe_{0.5} sample aged at 60 °C vs. 25 °C quantitatively indicate that temperature determines the extent of Fe being redeposited in the form of Fe oxides.

For the Fe_{0.5} catalyst, both its low bulk Fe content and the initial Fe atomic dispersion explain that some leached Fe atoms do not reprecipitate but remain dissolved and diffuse outside the thin-film electrode in the bulk electrolyte. For Fe_{5.0}, in contrast, both its ten-time higher Fe bulk content and the initial presence of Fe₃C NPs favour high local Fe cation concentration near the interface during AST, leading to fast reprecipitation of Fe cations as ferric oxides on top of Fe₃C particles.

While the results are unambiguous when it comes to the mild carbon corrosion in alkaline medium for these two Fe-N-C catalysts and on the fate of Fe during the AST, the possible catalytic role of the formed Fe oxides on the ORR is more complex to assess, due to their coexistence with a significant amount of (i) non-oxidized Fe₃C NPs remaining after AST for Fe_{5.0}, and of (ii) Fe-N_xC_y sites for Fe_{0.5}. The challenge to quantitatively assess how much Fe is present as Fe-N_xC_y sites / unoxidized Fe₃C NPs in aged Fe_{0.5} / Fe_{5.0} and how much is present as Fe oxide also contributes to the complexity of analysing the possible catalytic contribution of the *operando* formed Fe oxides with respect to the initially present ORR-active Fe sites. For Fe_{5.0}, the significant presence of Fe₃C NPs free of oxide shell and the concomitant decrease of 30–40% ORR activity (without any significant change in the Tafel slope) suggests that most of the activity loss results from two effects: a lowering of the turnover frequency for ORR via the formation of an iron oxide shell over some initially electrolyte-exposed Fe₃C NPs, and a decreasing ORR-active surface area through the dissolution of other Fe₃C NPs that were initially surrounded by a defective porous graphite shell.

For Fe_{0.5}, the small decrease in ORR activity at 0.85 V after AST despite 68% of all the Fe-N₄ sites situated on the surface initially has been leached in the electrolyte is intriguing, and suggests that a second active site may have formed. Combining ICP-MS analyses of the electrolyte and X-EDS analyses on particle-free regions of the thin-film, we conclude that roughly one half of Fe-N_xC_y sites survived the AST, one sixth was leached into the electrolyte, and one third reprecipitated in the thin film as Fe oxide (0.45 wt%, corresponding to 3.6 μg_{Fe} (of Fe oxide) cm⁻²_{geo}). While Fe oxides are known to have some ORR activity in alkaline medium, [77] previous works on Fe oxide supported on carbon do not suggest that such a low amount of Fe oxide could by itself account for a significant fraction of the ORR activity of Fe_{0.5} after the AST. However, the significant change in Tafel slope from 79 ± 1 mV decade⁻¹ to 107 ± 40 mV decade⁻¹ for Fe_{0.5} before/after [0.6–1.0 V – 3 s/3 s – 10 k – O₂ – 60 °C] and the resulting more pronounced loss of ORR activity at high overpotential (Table S3) identify a change in mechanism. The low amount of Fe oxide NP formed *in situ* in this case may work in

synergy with the remaining Fe-N_xC_y sites. Such a synergy was evoked for a model surface made of FeO_x NPs deposited on Fe-phthalocyanine (Fe-Pc) crystals supported on graphene [78]. The authors reported that the FeO_x/Fe-Pc/G composite surfaces (with 10 wt% or more of FeO_x) were significantly more active than the Fe-Pc/G surface, and far more active than the FeO_x/G surface. The synergy between FeO_x NPs and Fe-Pc was proposed to be related to the improved reversibility of the Fe(III)/Fe(II) redox peak of Fe-Pc in the presence of FeO_x NPs. While the estimated maximum amount of FeO_x NP on Fe_{0.5} (0.45 wt%) is far lower than in the above-mentioned work on model FeO_x/Fe-Pc surfaces, the surface chemistries are otherwise similar, supporting that an analogous synergetic effect between FeO_x and Fe-N_xC_y sites takes place in our case. Similar synergy was proposed by Feng *et al.* [79] who prepared Fe₂O₃ NPs supported on high surface area carbon. Those Fe₂O₃ NPs were then thermally treated, leading to Fe NPs, Fe₂O₃ NPs or a mix of Fe, Fe₂O₃ and Fe₃C NPs supported on carbon. The composite material performed better than the individual Fe phases. This result was accounted for by considering change in the electronic structure of Fe₃C NPs by the formed Fe₂O₃ NPs (electron withdrawing effect of Fe₂O₃). It was also suggested that multiple valence states and polymorphism of Fe₂O₃ facilitate O=O bond cleavage. In addition to a possible synergy between different Fe phases, the small but discernible ORR activity of N-doped carbon supports in alkaline is also worth pointing out. Gan *et al.* [80] recently synthesized a composite catalyst simultaneously containing Fe₂O₃-NPs/Fe-N_xC_y moieties encapsulated/embedded into multi-cage carbon spheres (Fe₂O₃/MCCS) or N-doped multi-cage carbon spheres (Fe₂O₃/N-MCCS). A decrease in the ORR activity (both half-wave potential and O₂ diffusion-limited current) was observed after acid-leaching or poisoning the Fe₂O₃/N-MCCS catalysts with cyanide ions (these treatments are supposed to dissolve/poison the Fe atoms, respectively), yet the residual ORR activity remained higher than that of Fe₂O₃/MCCS catalyst, pointing towards possible synergetic interactions between the N-doped support and the different Fe phases.

5. Conclusion

In summary, our results shed fundamental light into the mild carbon corrosion in alkaline medium for Fe-N-C catalysts, but also revealed electrochemical transformations occurring on single Fe atom catalysts and Fe carbide nanoparticles in alkaline ORR conditions. By combining advanced physical, chemical and electrochemical techniques, we provided comprehensive evidence of a previously undisclosed Fe dissolution/Fe oxide reprecipitation mechanism. The results suggest that the redeposited Fe oxide particles possibly act in synergy with the untransformed Fe-N_xC_y moieties, translating into a mild change of the apparent activity of the electrode after AST. In contrast, Fe oxide shells on Fe carbide core seem less active than the native Fe carbide particles. We thus propose the following guidelines to maximize the ORR activity/stability of Fe-N-C materials in alkaline electrolyte: for Fe-N-C catalysts based on core-shell particles (Fe@N-C), further improved stability can be reached if all the Fe carbide particles are surrounded by a defect-free graphite shell. For Fe-N-C catalysts based on single atom sites (Fe-N_xC_y), even higher initial ORR activity and higher stability can be reached by tailoring the synthesis and optimising the content of FeO_x NPs on a N-C matrix comprising single Fe atom sites. Besides their practical interest, these findings also illustrate that *operando* characterization of atomic/nanometre-scale Fe-N-C catalysts is of prime importance to establish reliable structure-chemistry-performance relationships.

CRediT authorship contribution statement

Ricardo Sgarbi: Sample collection and analysis; Investigation; Formal analysis; Drawing; Data curation; Writing – original draft. **Kavita Kumar:** Sample collection and analysis; Investigation; Formal analysis; Drawing; Data curation. **Viktoriia A. Saveleva:** X-ray absorption spectroscopy and X-ray emission spectroscopy measurements;

Formal analysis; Data curation. **Laetitia Dubau:** STEM/X-EDS measurements; Formal analysis; Data curation. **Raphaël Chattot:** WAXS measurements; Formal analysis. **Vincent Martin:** Methodology; ICP-MS measurements; Formal analysis; Data curation. **Michel Mermoux:** Raman spectroscopy measurements; Formal analysis. **Pierre Bordet:** Methodology; PDF analysis. **Pieter Glatzel:** X-ray absorption spectroscopy and X-ray emission spectroscopy measurements; Formal analysis; Data curation. **Edson A. Ticianelli:** Funding acquisition; Supervision. **Frédéric Jaouen:** Funding acquisition; Project administration; Resources; Validation, Writing – review & editing. **Frédéric Maillard:** Conceptualization; Data curation; Drawing; Formal analysis; Funding acquisition; Methodology; Project administration; Resources; Supervision; Validation; Visualization; Writing – review & editing.

Declaration of Competing Interest

The authors declare that they have no known competing financial interests or personal relationships that could have appeared to influence the work reported in this paper.

Acknowledgements

This work was performed within the framework of the Centre of Excellence of Multifunctional Architected Materials “CEMAM” no ANR-10-LABX-44-01. The authors thank the European Synchrotron Radiation facility for provision of synchrotron radiation facilities at beamline ID06, and gratefully acknowledge financial support from the French National Research Agency through the ANIMA (grant number ANR-19-CE05-0039) and DEEP (grant number ANR-21-CE05-0021) projects. R.S. acknowledges Coordenação de Aperfeiçoamento de Pessoal de Nível Superior (CAPES), Brazil (grant number 1614344) and CAPES/COFECUB program (grant numbers: 88887-187755/2018-00 and Ph-C 914/18). R.S. and E.A.T. are thankful to the São Paulo State Research Foundation (FAPESP – grant number: 2019/22183-6). Dr. R. Sgarbi and Dr. K. Kumar contributed equally to this work.

Appendix A. Supporting information

Supplementary data associated with this article can be found in the online version at doi:10.1016/j.apcatb.2022.121366.

References

- [1] L. Dubau, M. Lopez-Haro, L. Castanheira, J. Durst, M. Chatenet, P. Bayle-Guillemaud, L. Guétaz, N. Caqué, E. Rossinot, F. Maillard, Probing the structure, the composition and the ORR activity of Pt₃Co/C nanocrystallites during a 3422h PEMFC ageing test, *Appl. Catal. B Environ.* 142–143 (2013) 801–808, <https://doi.org/10.1016/j.apcatb.2013.06.011>.
- [2] M. Lopez-Haro, L. Dubau, L. Guétaz, P. Bayle-Guillemaud, M. Chatenet, J. André, N. Caqué, E. Rossinot, F. Maillard, Atomic-scale structure and composition of Pt₃Co/C nanocrystallites during real PEMFC operation: a STEM-EELS study, *Appl. Catal. B Environ.* 152 153 (2014) 300–308, <https://doi.org/10.1016/j.apcatb.2014.01.034>.
- [3] L. Dubau, F. Maillard, M. Chatenet, J. André, E. Rossinot, Nanoscale compositional changes and modification of the surface reactivity of Pt₃Co/C nanoparticles during proton-exchange membrane fuel cell operation, *Electrochim. Acta* 56 (2010) 776–783, <https://doi.org/10.1016/j.electacta.2010.09.038>.
- [4] L. Dubau, T. Asset, R. Chattot, C. Bonnaud, V. Vanpeene, J. Nelayah, F. Maillard, Tuning the performance and the stability of porous hollow PtNi/C nanostructures for the oxygen reduction reaction, *ACS Catal.* 5 (2015) 5333–5341, <https://doi.org/10.1021/acscatal.5b01248>.
- [5] S. Henning, L. Kühn, J. Herranz, J. Durst, T. Binninger, M. Nachttegaal, M. Werheid, W. Liu, M. Adam, S. Kaskel, A. Eychemüller, T.J. Schmidt, Pt-Ni aerogels as unsupported electrocatalysts for the oxygen reduction reaction, *J. Electrochem. Soc.* 163 (2016) F998–F1003, <https://doi.org/10.1149/2.0251609jes>.
- [6] S.M. Alia, C. Ngo, S. Shulda, M.A. Ha, A.A. Dameron, J.N. Weker, K.C. Neyerlin, S. S. Kocha, S. Pylypenko, B.S. Pivovar, Exceptional oxygen reduction reaction activity and durability of platinum-nickel nanowires through synthesis and post-treatment optimization, *ACS Omega* 2 (2017) 1408–1418, <https://doi.org/10.1021/acsomega.7b00054>.
- [7] T. Asset, R. Chattot, M. Fontana, B. Mercier-Guyon, N. Job, L. Dubau, F. Maillard, A review on recent developments and prospects for the oxygen reduction reaction

- on hollow Pt-alloy nanoparticles, *ChemPhysChem* 19 (2018) 1552–1567, <https://doi.org/10.1002/cphc.201800153>.
- [8] M. Escudero-Escribano, A. Verdager-Casadevall, P. Malacrida, U. Grönberg, B. P. Knudsen, A.K. Jepsen, J. Rossmeisl, I.E.L. Stephens, I. Chorkendorff, Pt₅Gd as a highly active and stable catalyst for oxygen electroreduction, *J. Am. Chem. Soc.* 134 (2012) 16476–16479, <https://doi.org/10.1021/ja306348d>.
 - [9] M. Escudero-Escribano, P. Malacrida, H.M. Hansen, U. Vej-Hansen, A. Velazquez-Palenzuela, V. Tripkovic, J. Schiotz, J. Rossmeisl, I.E.L. Stephens, I. Chorkendorff, Tuning the activity of Pt alloy electrocatalysts by means of the lanthanide contraction, *Science* 352 (2016) 73–76.
 - [10] J. Fichtner, B. Garlyyev, S. Watzele, H.A. El-Sayed, J.N. Schwämmlein, W.J. Li, F. M. Maillard, L. Dubau, J. Michalická, J.M. Macak, A. Holleitner, A.S. Bandarenka, Top-down synthesis of nanostructured platinum-lanthanide alloy oxygen reduction reaction catalysts: Pt₅Pr/C as an example, *ACS Appl. Mater. Interfaces* 11 (2019) 5129–5135, <https://doi.org/10.1021/acsami.8b20174>.
 - [11] C. Roy, B.P. Knudsen, C.M. Pedersen, A. Velázquez-Palenzuela, L.H. Christensen, C. D. Damsgaard, I.E.L. Stephens, I. Chorkendorff, Scalable synthesis of carbon-supported platinum-lanthanide and -rare-Earth alloys for oxygen reduction, *ACS Catal.* 8 (2018) 2071–2080, <https://doi.org/10.1021/acscatal.7b03972>.
 - [12] F.T. Wagner, B. Lakshmanan, M.F. Mathias, Electrochemistry and the future of the automobile, *J. Phys. Chem. Lett.* 1 (2010) 2204–2219, <https://doi.org/10.1021/jz100553m>.
 - [13] U. Martinez, S. Komini Babu, E.F. Holby, H.T. Chung, X. Yin, P. Zelenay, Progress in the development of Fe-based PGM-free electrocatalysts for the oxygen reduction reaction, *Adv. Mater.* 31 (2019) 1806545, <https://doi.org/10.1002/adma.201806545>.
 - [14] E. Guilminot, A. Corcella, F. Charlot, F. Maillard, M. Chatenet, Detection of Pt²⁺ ions and Pt nanoparticles inside the membrane of a used PEMFC, *J. Electrochem. Soc.* 154 (2007) B96–B105, <https://doi.org/10.1149/1.2388863>.
 - [15] E. Guilminot, A. Corcella, M. Chatenet, F. Maillard, F. Charlot, G. Berthomé, C. Iojoiu, J.-Y. Sanchez, E. Rossinot, E. Claude, Membrane and active layer degradation upon PEMFC steady-state operation, *J. Electrochem. Soc.* 154 (2007) B1106–B1114, <https://doi.org/10.1149/1.2775218>.
 - [16] L. Dubau, F. Maillard, M. Chatenet, L. Guetaz, J. André, E. Rossinot, Durability of Pt₃Co/C cathodes in a 16 cell PEMFC stack: Macro/microstructural changes and degradation mechanisms, *J. Electrochem. Soc.* 157 (2010) B1887, <https://doi.org/10.1149/1.3485104>.
 - [17] L. Dubau, L. Castanheira, G. Berthomé, F. Maillard, An identical-location transmission electron microscopy study on the degradation of Pt/C nanoparticles under oxidizing, reducing and neutral atmosphere, *Electrochim. Acta* 110 (2013) 273–281, <https://doi.org/10.1016/j.electacta.2013.03.184>.
 - [18] T. Asset, N. Job, Y. Busby, A. Crisci, V. Martin, V. Stergiopoulos, C. Bonnaud, A. Serov, P. Atanassov, R. Chattot, L. Dubau, F. Maillard, Porous hollow PtNi/C electrocatalysts: carbon support considerations to meet performance and stability requirements, *ACS Catal.* 8 (2018) 893–903, <https://doi.org/10.1021/acscatal.7b03539>.
 - [19] K. Kumar, P. Gairola, M. Lions, N. Ranjbar-Sahraie, M. Mermoux, L. Dubau, A. Zitolo, F. Jaouen, F. Maillard, Physical and chemical considerations for improving catalytic activity and stability of non-precious-metal oxygen reduction reaction catalysts, *ACS Catal.* 8 (2018) 11264–11276, <https://doi.org/10.1021/acscatal.8b02934>.
 - [20] K. Kumar, L. Dubau, M. Mermoux, J. Li, A. Zitolo, J. Nelayah, F. Jaouen, F. Maillard, On the influence of oxygen on the degradation of Fe-N-C catalysts, *Angew. Chemie Int. Ed.* (2020) 3235–3243, <https://doi.org/10.1002/anie.201912451>.
 - [21] A. Serov, I.V. Zhenyuk, C.G. Argers, M. Chatenet, Hot topics in alkaline exchange membrane fuel cells, *J. Power Sources* 375 (2018) 149–157, <https://doi.org/10.1016/j.jpowsour.2017.09.068>.
 - [22] L. Castanheira, L. Dubau, M. Mermoux, G. Berthomé, N. Cagué, E. Rossinot, M. Chatenet, F. Maillard, Carbon corrosion in proton-exchange membrane fuel cells: from model experiments to real-life operation in membrane electrode assemblies, *ACS Catal.* 4 (2014) 2258–2267, <https://doi.org/10.1021/cs500449q>.
 - [23] L. Castanheira, W.O. Silva, F.H.B. Lima, A. Crisci, L. Dubau, F. Maillard, Carbon corrosion in proton-exchange membrane fuel cells: Effect of the carbon structure, the degradation protocol, and the gas atmosphere, *ACS Catal.* 5 (2015) 2184–2194, <https://doi.org/10.1021/cs501973j>.
 - [24] N. Ramaswamy, S. Mukerjee, Fundamental mechanistic understanding of electrocatalysis of oxygen reduction on Pt and non-Pt surfaces: Acid versus alkaline media, *Adv. Phys. Chem.* 12 (2012) 1–17, <https://doi.org/10.1155/2012/491604>.
 - [25] R. Sgarbi, K. Kumar, F. Jaouen, A. Zitolo, E.A. Ticianelli, F. Maillard, Oxygen reduction reaction mechanism and kinetics on M-N₂C₂ and M@N-C active sites present in model M-N-C catalysts under alkaline and acidic conditions, *J. Solid State Electrochem.* 25 (2021) 45–56, <https://doi.org/10.1007/s10008-019-04436-w>.
 - [26] D. Chen, J. Ji, Z. Jiang, M. Ling, Z. Jiang, X. Peng, Molecular-confinement synthesis of sub-nano Fe/N/C catalysts with high oxygen reduction reaction activity and excellent durability for rechargeable Zn-Air batteries, *J. Power Sources* 450 (2020), 227660, <https://doi.org/10.1016/j.jpowsour.2019.227660>.
 - [27] Y. Gao, Z. Cai, X. Wu, Z. Lv, P. Wu, C. Cai, Graphdiyne-supported single-atom-sized Fe catalysts for the oxygen reduction reaction: DFT predictions and experimental validations, *ACS Catal.* 8 (2018) 10364–10374, <https://doi.org/10.1021/acscatal.8b02360>.
 - [28] Y. Chen, Z. Li, Y. Zhu, D. Sun, X. Liu, L. Xu, Y. Tang, Atomic Fe dispersed on N-doped carbon hollow nanospheres for high-efficiency electrocatalytic oxygen reduction, *Adv. Mater.* 31 (2019) 1806312, <https://doi.org/10.1002/adma.201806312>.
 - [29] X. Zhang, Y. Bahari, D. Lyu, L. Liang, F. Yu, M. Qing, Molecular-level design of Fe-N-C catalysts derived from Fe-dual pyridine coordination complexes for highly efficient oxygen reduction, *J. Catal.* 372 (2019) 245–257, <https://doi.org/10.1016/j.jcat.2019.03.003>.
 - [30] G.A. Ferrero, K. Preuss, A. Marinovic, A.B. Jorge, N. Mansor, D.J.L. Brett, A. B. Fuertes, M. Sevilla, M.M. Titirici, Fe-N-Doped carbon capsules with outstanding electrochemical performance and stability for the oxygen reduction reaction in both acid and alkaline conditions, *ACS Nano* 10 (2016) 5922–5932, <https://doi.org/10.1021/acsnano.6b01247>.
 - [31] W. Zhong, Z. Wang, S. Han, L. Deng, J. Yu, Y. Lin, X. Long, M. Gu, S. Yang, Identifying the active sites of a single atom catalyst with pH-universal oxygen reduction reaction activity, *Cell Rep. Phys. Sci.* 1 (2020), 100115, <https://doi.org/10.1016/j.xcrp.2020.100115>.
 - [32] G. Chen, P. Liu, Z. Liao, F. Sun, Y. He, H. Zhong, T. Zhang, E. Zschech, M. Chen, G. Wu, J. Zhang, X. Feng, Zinc-mediated template synthesis of Fe-N-C electrocatalysts with densely accessible Fe-N_x active sites for efficient oxygen reduction, *Adv. Mater.* 32 (2020) 1907399, <https://doi.org/10.1002/adma.201907399>.
 - [33] R. Sgarbi, E.A. Ticianelli, F. Maillard, F. Jaouen, M. Chatenet, Oxygen reduction reaction on metal and nitrogen – Doped carbon electrocatalysts in the presence of sodium borohydride, *Electrocatalysis* 11 (2020) 365–373, <https://doi.org/10.1007/s12678-020-00602-1>.
 - [34] T. Reshetyenko, V. Laue, U. Krewer, K. Artyushkova, Study of degradation and spatial performance of low Pt-loaded proton exchange membrane fuel cells under exposure to sulfur dioxide in an oxidant stream, *J. Power Sources* 458 (2020), 228032, <https://doi.org/10.1016/j.jpowsour.2020.228032>.
 - [35] B.P. Setzler, Z. Zhuang, J.A. Wittkopf, Y. Yan, Activity targets for nanostructured platinum-group-metal-free catalysts in hydroxide exchange membrane fuel cells, *Nat. Nanotechnol.* 11 (2016) 1020–1025, <https://doi.org/10.1038/nnano.2016.265>.
 - [36] J.R. Varcoe, P. Atanassov, D.R. Dekel, A.M. Herring, M.A. Hickner, P.A. Kohl, A. R. Kucernak, W.E. Mustain, K. Nijmeijer, K. Scott, T. Xu, L. Zhuang, Anion-exchange membranes in electrochemical energy systems, *Energy Environ. Sci.* 7 (2014) 3135–3191, <https://doi.org/10.1039/c4ee01303d>.
 - [37] D.R. Dekel, Review of cell performance in anion exchange membrane fuel cells, *J. Power Sources* 375 (2018) 158–169, <https://doi.org/10.1016/j.jpowsour.2017.07.117>.
 - [38] H. Adabi, A. Shakouri, N. Ul Hassan, J.R. Varcoe, B. Zulevi, A. Serov, J. R. Regalbuto, W.E. Mustain, High-performing commercial Fe-N-C cathode electrocatalyst for anion-exchange membrane fuel cells, *Nat. Energy* 6 (2021) 834–843, <https://doi.org/10.1038/s41560-021-00878-7>.
 - [39] P.G. Santori, F.D. Speck, S. Cherevko, H.A. Firouzjaie, X. Peng, W.E. Mustain, F. Jaouen, High performance FeNC and Mn-oxide/FeNC layers for AEMFC cathodes, *J. Electrochem. Soc.* 167 (2020), <https://doi.org/10.1149/1945-7111/abb7e0>.
 - [40] A. Ohma, K. Shinohara, A. Iiyama, T. Yoshida, A. Daimaru, Membrane and catalyst performance targets for automotive fuel cells by FCCJ membrane, catalyst, MEA WG, *ECRS Trans.* 41 (2011) 775–784, <https://doi.org/10.1149/1.3635611>.
 - [41] A. Zadick, L. Dubau, N. Sergeant, G. Berthomé, M. Chatenet, Huge instability of Pt/C catalysts in alkaline medium, *ACS Catal.* 5 (2015) 4819–4824, <https://doi.org/10.1021/acscatal.5b01037>.
 - [42] C. Lafforgue, M. Chatenet, L. Dubau, D.R. Dekel, Accelerated stress test of Pt/C nanoparticles in an interface with an anion-exchange membrane - an identical-location transmission electron microscopy study, *ACS Catal.* 8 (2018) 1278–1286, <https://doi.org/10.1021/acscatal.7b04055>.
 - [43] C. Lafforgue, F. Maillard, V. Martin, L. Dubau, M. Chatenet, Degradation of carbon-supported platinum-group-metal electrocatalysts in alkaline media studied by *in situ* Fourier transform infrared spectroscopy and identical-location transmission electron microscopy, *ACS Catal.* 9 (2019) 5613–5622, <https://doi.org/10.1021/acscatal.9b00439>.
 - [44] A. Zadick, L. Dubau, K. Artyushkova, A. Serov, P. Atanassov, M. Chatenet, Nickel-based electrocatalysts for ammonia borane oxidation: enabling materials for carbon-free-fuel direct liquid alkaline fuel cell technology, *Nano Energy* 37 (2017) 248–259, <https://doi.org/10.1016/j.nanoen.2017.05.035>.
 - [45] A. Mufundirwa, G.F. Harrington, B. Smid, B.V. Cuning, K. Sasaki, S.M. Lyth, Durability of template-free Fe-N-C foams for electrochemical oxygen reduction in alkaline solution, *J. Power Sources* 375 (2018) 244–254, <https://doi.org/10.1016/j.jpowsour.2017.07.025>.
 - [46] P.G. Santori, F.D. Speck, J. Li, A. Zitolo, Q. Jia, S. Mukerjee, S. Cherevko, F. Jaouen, Effect of pyrolysis atmosphere and electrolyte pH on the oxygen reduction activity, stability and spectroscopic signature of FeN_x moieties in Fe-N-C catalysts, *J. Electrochem. Soc.* 166 (2019) F3311–F3320, <https://doi.org/10.1149/2.0371907jes>.
 - [47] J. Sanetuntikul, S. Shanmugam, High pressure pyrolyzed non-precious metal oxygen reduction catalysts for alkaline polymer electrolyte membrane fuel cells, *Nanoscale* 7 (2015) 7644–7650, <https://doi.org/10.1039/c5nr00311c>.
 - [48] H. Tan, Y. Li, J. Kim, T. Takei, Z. Wang, X. Xu, J. Wang, Y. Bando, Y.M. Kang, J. Tang, Y. Yamauchi, Sub-50 nm iron-nitrogen-doped hollow carbon sphere-encapsulated iron carbide nanoparticles as efficient oxygen reduction catalysts, *Adv. Sci.* 5 (2018), <https://doi.org/10.1002/advs.201800120>.
 - [49] M. Thomas, R. Ilathvalappil, S. Kurungot, B.N. Nair, A.P. Mohamed, G. M. Anilkumar, T. Yamaguchi, U.S. Hareesh, Morphological ensembles of N-doped porous carbon derived from ZIF-8/Fe-graphene nanocomposites: processing and

- electrocatalytic studies, *ChemistrySelect* 3 (2018) 8688–8697, <https://doi.org/10.1002/slct.201801419>.
- [50] Z. Yan, C. Dai, M. Zhang, X. Lv, X. Zhao, J. Xie, Nitrogen doped porous carbon with iron promotion for oxygen reduction reaction in alkaline and acidic media, *Int. J. Hydrog. Energy* 44 (2019) 4090–4101, <https://doi.org/10.1016/j.ijhydene.2018.12.180>.
- [51] S.G. Peera, J. Balamurugan, N.H. Kim, J.H. Lee, Sustainable synthesis of Co@NC core shell nanostructures from metal organic frameworks via mechanochemical coordination self-assembly: An efficient electrocatalyst for oxygen reduction reaction, *Small* 14 (2018) 1800441, <https://doi.org/10.1002/smll.201800441>.
- [52] Á. García, L. Pascual, P. Ferrer, D. Gianolio, G. Held, D.C. Grinter, M.A. Peña, M. Retuerto, S. Rojas, Study of the evolution of FeN_xC_y and Fe₃C species in Fe/N/C catalysts during the oxygen reduction reaction in acid and alkaline electrolyte, *J. Power Sources* 490 (2021), <https://doi.org/10.1016/j.jpowsour.2021.229487>.
- [53] C. Domínguez, F.J. Pérez-Alonso, M.A. Salam, S.A. Al-Thabaiti, M.A. Peña, F. J. García-García, L. Barrio, S. Rojas, Repercussion of the carbon matrix for the activity and stability of Fe/N/C electrocatalysts for the oxygen reduction reaction, *Appl. Catal. B Environ.* 183 (2016) 185–196, <https://doi.org/10.1016/j.apcatb.2015.10.043>.
- [54] S.H. Lee, J. Kim, D.Y. Chung, J.M. Yoo, H.S. Lee, M.J. Kim, B.S. Mun, S.G. Kwon, Y. E. Sung, T. Hyeon, Design principle of Fe–N–C electrocatalysts: How to optimize multimodal porous structures? *J. Am. Chem. Soc.* 141 (2019) 2035–2045, <https://doi.org/10.1021/jacs.8b11129>.
- [55] R. Gokhale, Y. Chen, A. Serov, K. Artyushkova, P. Atanassov, Novel dual templating approach for preparation of highly active Fe–N–C electrocatalyst for oxygen reduction, *Electrochim. Acta* 224 (2017) 49–55, <https://doi.org/10.1016/j.electacta.2016.12.052>.
- [56] A. Zitolo, N. Ranjbar-Sahraie, T. Mineva, J. Li, Q. Jia, S. Stamatini, G.F. Harrington, S.M. Lyth, P. Krti, S. Mukerjee, E. Fonda, F. Jaouen, Identification of catalytic sites in cobalt-nitrogen-carbon materials for the oxygen reduction reaction, *Nat. Commun.* 8 (2017) 957, <https://doi.org/10.1038/s41467-017-01100-7>.
- [57] G. Ashiotis, A. Deschildre, Z. Nawaz, J.P. Wright, D. Karkoulis, F.E. Picca, J. Kieffer, The fast azimuthal integration Python library: PyFAI, *J. Appl. Crystallogr.* 48 (2015) 510–519, <https://doi.org/10.1107/S1600576715004306>.
- [58] X. Qiu, J.W. Thompson, S.J.L. Billinge, PDFgetX2: a GUI-driven program to obtain the pair distribution function from X-ray powder diffraction data, *J. Appl. Crystallogr.* 37 (2004) 678, <https://doi.org/10.1107/S0021889804011744>.
- [59] A. Zitolo, V. Goellner, V. Armel, M.T. Sougrati, T. Mineva, L. Stievano, E. Fonda, F. Jaouen, Identification of catalytic sites for oxygen reduction in iron- and nitrogen-doped graphene materials, *Nat. Mater.* 14 (2015) 937–942, <https://doi.org/10.1038/nmat4367>.
- [60] V. Armel, J. Hannauer, F. Jaouen, Effect of ZIF-8 crystal size on the O₂ electro-reduction performance of pyrolyzed Fe–N–C catalysts, *Catalysts* 5 (2015) 1333–1351, <https://doi.org/10.3390/catal5031333>.
- [61] J. Li, M.T. Sougrati, A. Zitolo, J.M. Ablett, I.C. Oğuz, T. Mineva, I. Matanovic, P. Atanassov, Y. Huang, I. Zenyuk, A. Di Cicco, K. Kumar, L. Dubau, F. Maillard, G. Dražić, F. Jaouen, Identification of durable and non-durable FeN_x sites in Fe–N–C materials for proton exchange membrane fuel cells, *Nat. Catal.* 4 (2021) 10–19, <https://doi.org/10.1038/s41929-020-00545-2>.
- [62] V. Petkov, R.G. Difrancesco, S.J.L. Billinge, M. Acharya, H.C. Foley, Local structure of nanoporous carbons, *Philos. Mag. B* 79 (1999) 1519–1530, <https://doi.org/10.1080/13642819908218319>.
- [63] P. Glatzel, G. Smolentsev, G. Bunker, The electronic structure in 3d transition metal complexes: can we measure oxidation states? *J. Phys. Conf. Ser.* 190 (2009) 12046, <https://doi.org/10.1088/1742-6596/190/1/012046>.
- [64] S. Lafuerza, A. Carluantonio, M. Retegan, P. Glatzel, Chemical sensitivity of K β and K α X-ray emission from a systematic investigation of iron compounds, *Inorg. Chem.* 59 (2020) 12518–12535, <https://doi.org/10.1021/acs.inorgchem.0c01620>.
- [65] V.A. Saveleva, K. Ebner, L. Ni, G. Smolentsev, D. Klose, A. Zitolo, E. Marelli, J. Li, M. Medarde, O.V. Safonova, M. Nachttegaal, F. Jaouen, U.I. Kramm, T.J. Schmidt, J. Herranz, Potential-induced spin changes in Fe/N/C electrocatalysts assessed by *in situ* X-ray emission spectroscopy, *Angew. Chem. Int. Ed. Engl.* (2021), <https://doi.org/10.1002/anie.202016951>.
- [66] K. Kumar, T. Asset, X. Li, Y. Liu, X. Yan, Y. Chen, M. Mermoux, X. Pan, P. Atanassov, F. Maillard, L. Dubau, Fe–N–C electrocatalysts' durability: effects of single atoms' mobility and clustering, *ACS Catal.* 11 (2021) 484–494, <https://doi.org/10.1021/acscatal.0c04625>.
- [67] G. Bae, H. Kim, H. Choi, P. Jeong, D.H. Kim, H.C. Kwon, K.-S. Lee, M. Choi, H.-S. Oh, F. Jaouen, C.H. Choi, Quantification of active site density and turnover frequency: From single-atom metal to nanoparticle electrocatalysts, *JACS Au* 1 (2021) 586–597, <https://doi.org/10.1021/jacsau.1c00074>.
- [68] H. Adabi, P.G. Santori, A. Shakouri, X. Peng, K. Yassin, I.G. Rasin, S. Brandon, D. R. Dekel, N.U. Hassan, M.-T. Sougrati, A. Zitolo, J.R. Varcoe, J.R. Regalbuto, F. Jaouen, W.E. Mustain, Understanding how single-atom site density drives the performance and durability of PGM-free Fe–N–C cathodes in anion exchange membrane fuel cells, *Mater. Today Adv.* 12 (2021), 100179, <https://doi.org/10.1016/j.mtadv.2021.100179>.
- [69] A. Sadezky, H. Muckenhuber, H. Grothe, R. Niessner, U. Pöschl, Raman microspectroscopy of soot and related carbonaceous materials: Spectral analysis and structural information, *Carbon* N. Y 43 (2005) 1731–1742, <https://doi.org/10.1016/j.carbon.2005.02.018>.
- [70] J.S. Park, A. Reina, R. Saito, J. Kong, G. Dresselhaus, M.S. Dresselhaus, G' band Raman spectra of single, double and triple layer graphene, *Carbon* N. Y 47 (2009) 1303–1310, <https://doi.org/10.1016/j.carbon.2009.01.009>.
- [71] K. Kinoshita, *Carbon: Electrochemical and Physicochemical Properties*, John Wiley & Sons, Inc, New York, 1988.
- [72] V. Perazzolo, E. Grądzka, C. Durante, R. Pilot, N. Vicentini, G.A. Rizzi, G. Granozzi, A. Gennaro, Chemical and electrochemical stability of nitrogen and sulphur doped mesoporous carbons, *Electrochim. Acta* 197 (2016) 251–262, <https://doi.org/10.1016/j.electacta.2016.02.025>.
- [73] G. Bae, M.W. Chung, S.G. Ji, F. Jaouen, C.H. Choi, pH effect on the H₂O₂-induced deactivation of Fe–N–C catalysts, *ACS Catal.* 10 (2020) 8485–8495, <https://doi.org/10.1021/acscatal.0c00948>.
- [74] K.H. Gayer, L. Woontner, The solubility of ferrous hydroxide and ferric hydroxide in acidic and basic media at 25°, *J. Phys. Chem.* 60 (1956) 1569–1571, <https://doi.org/10.1021/j150545a021>.
- [75] M. Pourbaix, *Atlas of Electrochemical Equilibria in Aqueous Solutions*, National Association of Corrosion Engineers, Houston, 1974.
- [76] V. Goellner, C. Baldizzone, A. Schuppert, M.T. Sougrati, K.J.J. Mayrhofer, F. Jaouen, Degradation of Fe/N/C catalysts upon high polarization in acid medium, *Phys. Chem. Chem. Phys.* 16 (2014) 18454–18462, <https://doi.org/10.1039/c4cp02882a>.
- [77] Q. He, E.J. Cairns, Review—recent progress in electrocatalysts for oxygen reduction suitable for alkaline anion exchange membrane fuel cells, *J. Electrochem. Soc.* 162 (2015) F1504–F1539, <https://doi.org/10.1149/2.0551514jes>.
- [78] Y. Cheng, J. Liang, J.P. Veder, M. Li, S. Chen, J. Pan, L. Song, H.M. Cheng, C. Liu, S. P. Jiang, Iron oxide nanoclusters incorporated into iron phthalocyanine as highly active electrocatalysts for the oxygen reduction reaction, *ChemCatChem* 10 (2018) 475–483, <https://doi.org/10.1002/cctc.201701183>.
- [79] W. Feng, M. Liu, J. Liu, Y. Song, F. Wang, Well-defined Fe, Fe₃C, and Fe₂O₃ heterostructures on carbon black: a synergistic catalyst for oxygen reduction reaction, *Catal. Sci. Technol.* 8 (2018) 4900–4906, <https://doi.org/10.1039/C8CY01223G>.
- [80] R. Gan, Y. Wang, W. Ma, M. Dirican, S. Zhao, Y. Song, X. Zhang, C. Ma, J. Shi, Fe₂O₃-encapsulated and Fe–N_x-containing hierarchical porous carbon spheres as efficient electrocatalyst for oxygen reduction reaction, *Int. J. Hydrog. Energy* (2021), <https://doi.org/10.1016/j.ijhydene.2021.10.157>.